Nanoelectronics and Its New Materials – A NEW ERA OF NANOSCIENCE

Nanoelectronics and Its New Materials –

A NEW ERA OF NANOSCIENCE

ZEISS
Seeing beyond

WILEY

Discover the recent advances in electronics research and fundamental nanoscience.

Nanotechnology has become the driving force behind breakthroughs in engineering, materials science, physics, chemistry, and biological sciences. In this compendium, we delve into a wide range of novel applications that highlight recent advances in electronics research and fundamental nanoscience. From surface analysis and defect detection to tailored optical functionality and transparent nanowire electrodes, this eBook covers key topics that will revolutionize the future of electronics.

To get your hands on this valuable resource and unleash the power of nanotechnology, simply download the eBook now. Stay ahead of the curve and embrace the future of electronics with nanoscience as your guide.

ZEISS
Seeing beyond

WILEY

In Situ Oxygen Doping of Monolayer MoS$_2$ for Novel Electronics

Jian Tang, Zheng Wei, Qinqin Wang, Yu Wang, Bo Han, Xiaomei Li, Biying Huang, Mengzhou Liao, Jieying Liu, Na Li, Yanchong Zhao, Cheng Shen, Yutuo Guo, Xuedong Bai, Peng Gao, Wei Yang, Lan Chen, Kehui Wu, Rong Yang,* Dongxia Shi, and Guangyu Zhang*

In 2D semiconductors, doping offers an effective approach to modulate their optical and electronic properties. Here, an in situ doping of oxygen atoms in monolayer molybdenum disulfide (MoS$_2$) is reported during the chemical vapor deposition process. Oxygen concentrations up to 20–25% can be reliable achieved in these doped monolayers, MoS$_{2-x}$O$_x$. These oxygen dopants are in a form of substitution of sulfur atoms in the MoS$_2$ lattice and can reduce the bandgap of intrinsic MoS$_2$ without introducing in-gap states as confirmed by photoluminescence spectroscopy and scanning tunneling spectroscopy. Field effect transistors made of monolayer MoS$_{2-x}$O$_x$ show enhanced electrical performances, such as high field-effect mobility (≈100 cm^2 V^{-1} s^{-1}) and inverter gain, ultrahigh devices' on/off ratio (>10^9) and small subthreshold swing value (≈80 mV dec^{-1}). This in situ oxygen doping technique holds great promise on developing advanced electronics based on 2D semiconductors.

1. Introduction

2D transition metal dichalcogenides (TMDs) are emerging low-dimensional materials with potential applications for optics and electronics.[1,2] Among many 2D-TMDs, 2H phase monolayer MoS$_2$ is a representative direct bandgap semiconductor with bandgap (E_g) of ≈2.2 eV and has been intensely explored as an alternative for high-performance thin film transistors and large-area integrated electronics.[3,4] In order to realize the full potential of 2D-MoS$_2$ in such applications, it requires to effectively modulate their electrical, optical, and structural properties by introducing impurities for doping.[5–10] So far, the chemisorption and charge transfer through surface functionalization are effective approaches to achieve doping, but it has a relatively weak influences on band structures or improvements of electronic properties.[11,12] By contrast, substitutional doping is more stable and capable of tailoring the bandgap of 2D-TMDs without introducing in-gap states.[13–16] Such substitutional doping could be realized through replacing the host transition metal or chalcogen atoms with other elements during synthesis to form alloys such as Mo$_{1-x}$W$_x$S$_2$, MoS$_{2x}$Se$_{2(1-x)}$, and V$_x$W$_y$Mo$_{1-x-y}$S$_{2z}$Se$_{2(1-z)}$, etc.[17–21]

Recently, oxygen doping of 2D-MoS$_2$ has attracted considerable research interests. Previous studies show that post treatments of intrinsic MoS$_2$ in air, ozone, or oxygen plasma could induce oxygen doping, evidenced from the enhanced catalytic reactivity, quenched photoluminescence, and improved electrical conductivity.[9,18,22–24] Such doping processes usually lead to oxygen substitution and oxidation as well and consequently yield highly disordered or fragmented lattice structures. In situ oxygen substitutional doping in 2D-MoS$_2$ with a controlled and nondestructive manner is thus highly desired to preserve its original lattice structure, but still remains challenging so far.

J. Tang, Z. Wei, Q. Wang, Y. Wang, Dr. X. Li, B. Huang, Dr. M. Liao, J. Liu, Dr. N. Li, Y. Zhao, Dr. C. Shen, Y. Guo, Prof. X. Bai, Prof. W. Yang, Prof. L. Chen, Prof. K. Wu, Prof. R. Yang, Prof. D. Shi, Prof. G. Zhang
Institute of Physics and Beijing National Laboratory for Condensed Matter Physics
Chinese Academy of Sciences
Beijing 100190, China
E-mail: ryang@iphy.ac.cn; gyzhang@iphy.ac.cn

J. Tang, Z. Wei, Q. Wang, Y. Wang, Dr. X. Li, B. Huang, J. Liu, Dr. N. Li, Y. Zhao, Dr. C. Shen, Y. Guo, Prof. X. Bai, Prof. W. Yang, Prof. L. Chen, Prof. K. Wu, Prof. D. Shi, Prof. G. Zhang
School of Physical Sciences
University of Chinese Academy of Sciences
Beijing 100190, China

Dr. B. Han, Dr. X. Li, Prof. P. Gao
Electron Microscopy Laboratory and International Center for Quantum Materials
School of Physics
Peking University
Beijing 100871, China

Dr. N. Li, Prof. W. Yang, Prof. L. Chen, Prof. K. Wu, Prof. R. Yang, Prof. G. Zhang
Songshan Lake Materials Laboratory
Dongguan, Guangdong 523808, China

Prof. W. Yang, Prof. R. Yang, Prof. D. Shi, Prof. G. Zhang
Beijing Key Laboratory for Nanomaterials and Nanodevices
Beijing 100190, China

ADVANCED
SCIENCE NEWS
www.advancedsciencenews.com

NANO · MICRO
small
www.small-journal.com

In this work, we demonstrated the in situ oxygen substitutional doping of monolayer MoS_2 in the chemical vapor deposition (CVD) growth process. By introducing oxygen gas in the growth environment, we can achieve uniform oxygen doping in monolayer MoS_2 with tunable dopant concentrations, i.e., $MoS_{2-x}O_x$, without changing the lattice ordering. We also show the creation of in-plane heterostructures of $MoS_{2-x}O_x$ with different doping levels by tuning the oxygen gas partial pressure during the growth process. The atomic and electronic structures of the $MoS_{2-x}O_x$ samples were systematically characterized by scanning tunneling microscopy (STM), scanning tunneling spectroscopy (STS), scanning transmission electron microscope (STEM), X-ray photoelectron spectroscopy (XPS), Raman spectroscopy, and photoluminescence (PL) spectroscopy. More importantly, we found that the bandgap of monolayer $MoS_{2-x}O_x$ can be tuned by the oxygen doping levels. Electrical measurements on the fabricated field effect transistors (FETs) and logic gates reveal that, at an optimized doping level (within 20% doping concentration), $MoS_{2-x}O_x$ monolayers feature excellent device performances including large current capacities, enhanced sheet conductance, and associated carrier mobilities. These superior electrical properties of monolayer $MoS_{2-x}O_x$ suggest their potentials for high performance and low power consumption electronics.

2. Results and Discussion

The in situ growth of $MoS_{2-x}O_x$ monolayers was performed in our home-made CVD system as illustrated in **Figure 1**a. MoO_3, S, and O_2 were used as reaction sources and the growth of $MoS_{2-x}O_x$ monolayers was achieved on preannealed c-plane sapphire substrates, which were vertically placed in the growth chamber. Such vertical placement is beneficial to achieve more uniform growth temperature and source flux homogeneity across the 2 in. substrate. Since the substrate directly faces to the evaporation sources, the growth rate is also increased as compared to the lateral growth. The synthesized $MoS_{2-x}O_x$ triangles are spatially uniform as comparing the synthesized $MoS_{2-x}O_x$ triangles with horizontal placed sapphire substrate (Figures S1–S3, Supporting Information). According to the designed reaction routes in Figure 1b,[25] we use Ar and Ar/O_2 carrier gases for S and MoO_3 sources independently during the growth. Note that O_2 carrier gas could not only balance the sulfurization capacity of S sources but also act as the oxygen doping source for growth of $MoS_{2-x}O_x$.[18,26,27] Besides, the growth temperature (T_G), i.e., the temperature of substrates, affects the doping process dominantly.[25,28] At $T_G > 900$ °C, sulfur has very strong sulfuration properties and MoO_3 can be totally sulfureted to MoS_2 with improved crystal quality, and oxygen doping process is
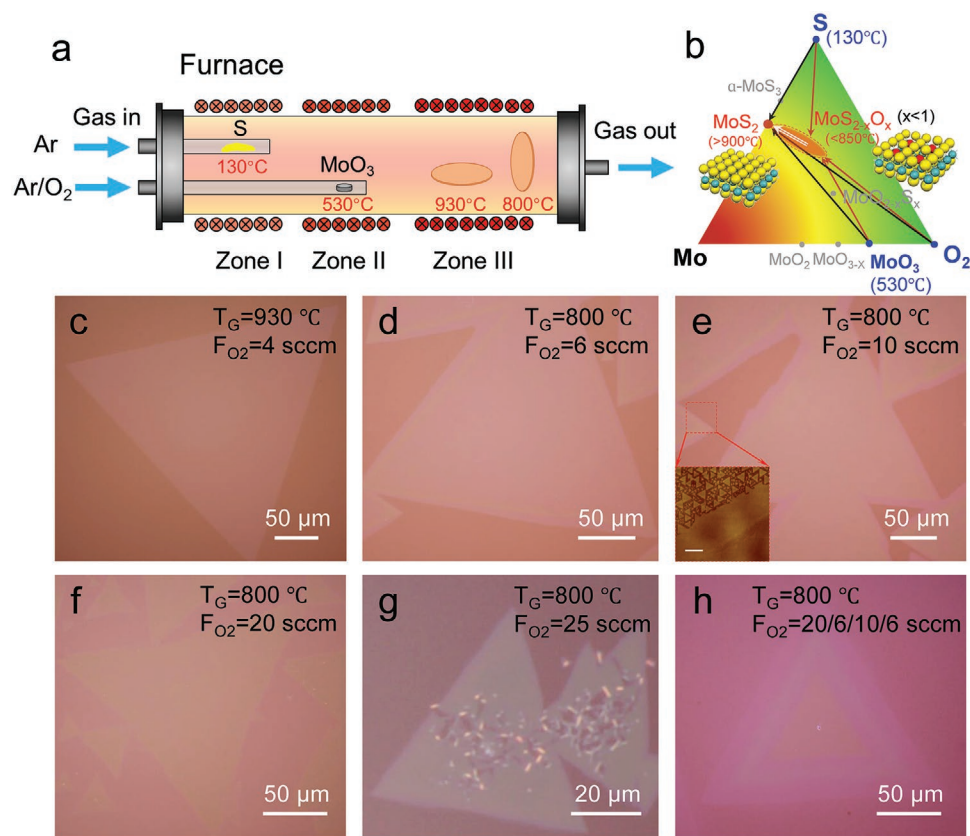

Figure 1. The growth of monolayer $MoS_{2-x}O_x$ films. a) Schematic set up of a three-temperature zone CVD system for synthesis monolayer $MoS_{2-x}O_x$ films. b) The phase diagram and designed reaction routes for synthesizing $MoS_{2-x}O_x$. c–g) Optical images of the synthesized $MoS_{2-x}O_x$ triangles with increasing doping levels by varying the oxygen carrier gas flow-rate (F_{O2}) from 4 to 25 sccm and growth temperature (T_G) from 930 to 800 °C. Inset in (e) is the AFM image across the boundary of $MoS_{2-x}O_x$ triangle. Scale bar, 1 µm. h) The controllable growth of $MoS_{2-x}O_x$ heterostructures with F_{O2} of 20/6/10/6 sccm at 800 °C.
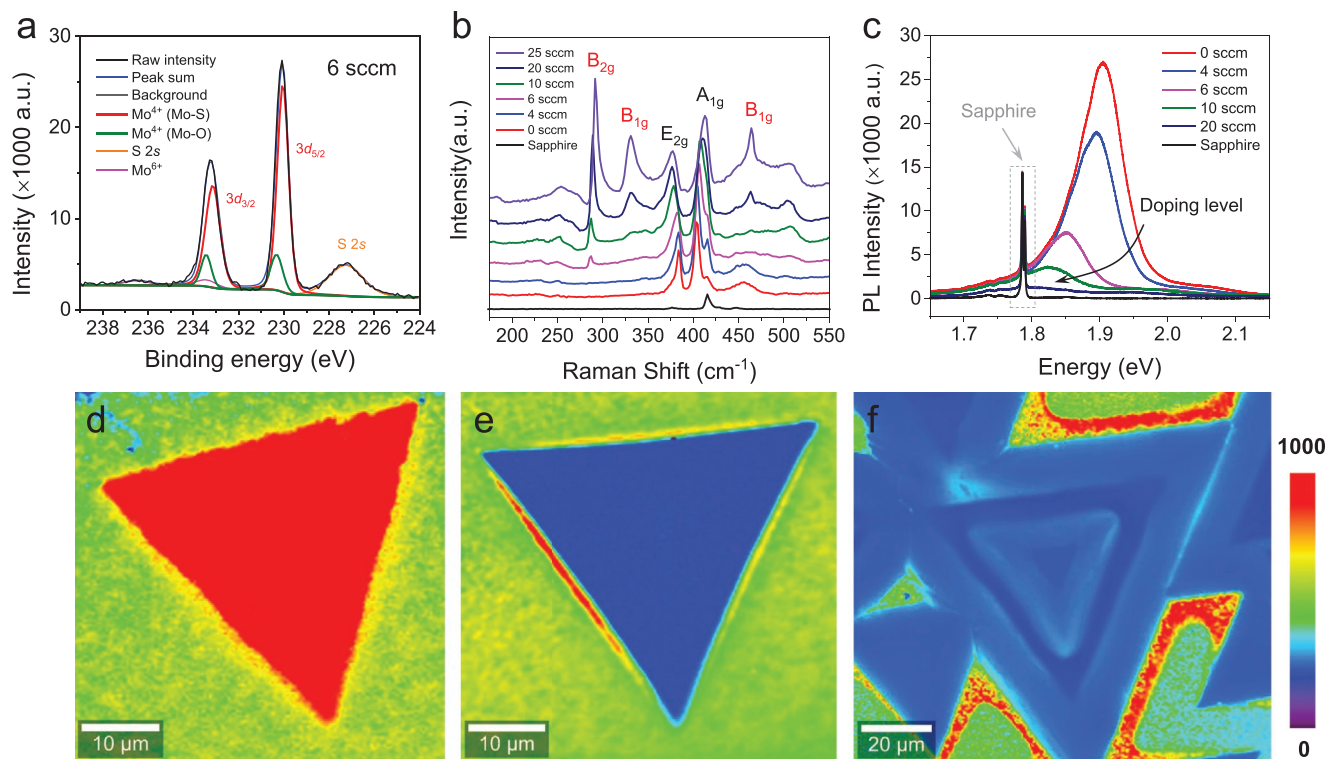
Figure 2. The optical properties characterizations of $MoS_{2-x}O_x$. a) XPS spectra of $MoS_{2-x}O_x$ synthesized with F_{O2} = 6 sccm. b,c) Raman and PL spectrum of $MoS_{2-x}O_x$ with increased oxygen doping levels. d–f) PL mapping of as-grown $MoS_{2-x}O_x$ samples synthesized with F_{O2} of 4 sccm (d), 10 sccm (e), and 20/6/10/6 sccm (f).

suppressed meanwhile, as comparing optical properties of the $MoS_{2-x}O_x$ samples synthesized with oxygen flow-rate (F_{O2}) from 0 to 20 sccm at 930 °C (Figures S4 and S5, Supporting Information). While the oxygen doping dopants can be reliably introduced and tuned at low T_G, e.g., T_G < 850 °C, by just varying F_{O2} (Figures S6 and S7, Supporting Information).

Figure 1c–g shows optical microscope images of typical as-grown $MoS_{2-x}O_x$ triangles obtained under different growth conditions. We can see that their optical contrasts accentuate with F_{O2}, suggesting the formation of $MoS_{2-x}O_x$. Clearer contrast can be found from their undoped outer edges which are grown during cooling down process when O_2 gas supply was switched off (Figure 1e). Atomic force microscope (AFM) imaging on these triangles shows no obvious height differences across the $MoS_{2-x}O_x/MoS_2$ boundaries (inset in Figure 1e; Figure S8, Supporting Information), and the 0.7 nm film thickness equals to a monolayer thickness. An excessive oxygen doping could lead to structural damages and etch the $MoS_{2-x}O_x$ basal plane during growth as shown in Figure 1g. This in situ oxygen doping approach can also be used to produce 2D heterostructures in desired locations with controlled dimensions. As shown in Figure 1h, we synthesized lateral heterostructure in the same $MoS_{2-x}O_x$ flake via spatially engineering the oxygen doping levels. The synthesized $MoS_{2-x}O_x$ heterostructure with sharp optical contrast was produced by sequential switching F_{O2} to be 20/6/10/6 sccm during the growth process at 800 °C.

We first performed X-ray photoemission spectroscopy (XPS) for semiqualitative analysis of the oxygen dopant concentrations of $MoS_{2-x}O_x$ samples as shown in **Figure 2**a and

Figure S9 (Supporting Information). The Mo 3d spectrum is fitted to the doublet peaks at 230 and 233.1 eV with ≈3.1 eV spin–orbit splitting, corresponding to Mo^{4+} peaks of Mo−S bonds, the doublet peaks at 230.2 and 233.3 eV, corresponding to Mo^{4+} peaks of Mo−O bonds, the doublet peaks at 233.2 and 236.3 eV, corresponding to Mo^{6+} peaks for MoO_3 compounds formed in oxygen-doped $MoS_{2-x}O_x$ samples.[29,30] Note that the peak at 227.3 eV corresponds to the binding energy of S 2s electrons. Thus, we can qualitatively estimate the amount of oxygen dopant concentrations by considering the peak areas of Mo^{4+} of Mo−O bonds and Mo−S bonds, and Mo^{6+} of MoO_3 as shown in **Table 1**. For the O_S concentrations (x), it follows 0%, 0%, 16.5%, 22.7%, 24.7%, and 26.1% for F_{O2} = 0, 4, 6, 10, 20, and 25 sccm $MoS_{2-x}O_x$ samples according to: S(Mo−O)/[S(Mo−O) + S(Mo−S)] of Mo^{4+} species. For the MoO_3 concentrations, it follows 0%, 0%, 5.5%, 10.5%, 17.2%, and 15.8% according to: S(Mo^{6+})/[S(Mo^{4+}) + S(Mo^{6+})].

Table 1. Oxygen dopant concentrations of $MoS_{2-x}O_x$.

F_{O2} [sccm]	T_G [°C]	O_S ratio [%]	MoO_3 ratio [%]
0	930	0	0
4	930	0	0
6	800	16.5	5.5
10	800	22.7	10.5
20	800	24.7	17.2
25	800	26.1	15.8

Then, we further carried out optical spectroscopy characterizations for these monolayer $MoS_{2-x}O_x$ samples with different doping concentrations as illustrated in Figure 1c–g. The Raman spectra are shown in Figure 2b. Beside E_{2g} and A_{1g} modes of intrinsic monolayer MoS_2, a series of new Raman vibration modes appear. The new peaks at 287 cm^{-1} (B_{2g}), 331 cm^{-1} (B_{1g}), and 464 cm^{-1} (B_{1g}), corresponding to the vibration modes of Mo—O bonds,[24,31] confirm the oxygen doping in monolayer MoS_2. According to Hardcastle's empirical relationship[32] between Mo—O bond length (R, Å) and Raman vibrational frequencies (v, cm^{-1}), which follows: $v(cm^{-1}) = 32895\exp(-2.073 \cdot R)$, based on diatomic approximation, we could estimate the Mo—O bond lengths of 2.29 Å from the first observed Raman vibrational frequencies at 287 cm^{-1}, which is close to Mo—S bond length (2.41 Å) in MoS_2 lattice with a ≈5% shortening. Thus, we assign the Raman peaks at 287 cm^{-1} to excellent estimates of the vibrational modes of Mo—O bonds for oxygen substitutional atoms in MoS_2 lattice. These new Raman peaks become more prominent with increased F_{O2}, which suggests an increased oxygen dopant concentration and indicates the gradually formation of MoO_3 areas at high oxygen dopant concentrations of $MoS_{2-x}O_x$ samples. Apart from these new modes, increased oxygen doping levels would induce gradual broadening and red/blue shifts of E_{2g}/A_{1g} vibration modes as shown in Figure 2b.[29] PL spectra of $MoS_{2-x}O_x$ samples with F_{O2} varying from 0 to 20 sccm were shown in Figure 2c. With the increased oxygen doping levels, the optical bandgap decreases from 1.9 eV at $F_{O2} = 0$ sccm to 1.82 eV at $F_{O2} = 10$ sccm, revealing a modulation of the bandgap by oxygen doping. Significant PL quenching is present when $F_{O2} > 10$ sccm. Note that the two prominent sharp PL peaks around 1.78 eV originate from sapphire substrate. Figure 2d–f shows the spatially resolved PL mapping of monolayer $MoS_{2-x}O_x$ triangles with F_{O2} of 4 and 10 sccm, as well as $MoS_{2-x}O_x$ heterostructure with F_{O2} of 20/6/10/6 sccm. The good uniformity of PL intensity in Figure 2d,e indicates the spatially homogeneous doping of the entire $MoS_{2-x}O_x$ triangles. Besides, the sharp PL intensity contrast of the synthesized $MoS_{2-x}O_x$ heterostructures (Figure 2f) indicates the successful synthesizing of in-plane $MoS_{2-x}O_x$ heterostructures with sharp boundaries. Thus, we are able to engineer the electronic structure of $MoS_{2-x}O_x$ by spatial modulation the oxygen dopant concentrations.

In order to reveal the atomic structure and local electronic properties of monolayer $MoS_{2-x}O_x$ samples, we thus performed STM/STS and STEM experiments. Monolayer $MoS_{2-x}O_x$ film was grown on the highly oriented pyrolytic graphite (HOPG) with $F_{O2} = 6$ sccm at 800 °C as shown in **Figure 3**a. Figure 3b,c shows typical atomic resolution STM images of monolayer $MoS_{2-x}O_x$ at different scanning scales. The uniformly distributed hexagonal halo patterns in Figure 3b are assigned to O_S substitutional sites in the MoS_2 crystal lattice, in agreement with previous reports.[15,16,18] Importantly, two different halo patterns having obvious contrasts than the background MoS_2 lattice are visualized. Our simulated STM images based on density-functional theory (DFT) calculations (details in the Experimental Section) show that these two features, i.e., the darker/brighter, correspond to substitutional O atom in the top/bottom S layer ($O_{S\text{-top}}/O_{S\text{-bottom}}$), as illustrated in the suggested atomic structures and simulated STM images in Figure 3d,e.
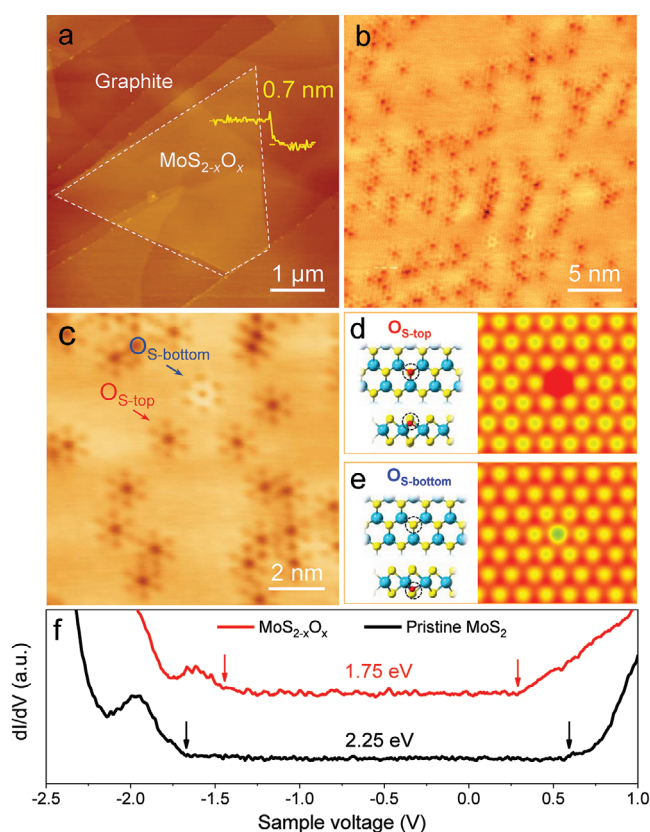

Figure 3. Atomic structure configuration and localized electronic properties of O_S in $MoS_{2-x}O_x$. a) AFM image of as-grown $MoS_{2-x}O_x$ on HOPG substrates ($F_{O2} = 6$ sccm, 800 °C). b,c) High-resolution STM images of $MoS_{2-x}O_x$ at different scale. Set points: 0.74 V, 100 pA (b); 0.8 V, 50 pA (c). The O_S could be distinguished by dark ($O_{S\text{-top}}$) or bright ($O_{S\text{-bottom}}$) hexagonal halo patterns. d,e) Simulated STM images of $O_{S\text{-top}}$ (d) and $O_{S\text{-bottom}}$ (e). Left panels correspond to top and side view of the DFT-calculated atomic structure and O_S sites are marked by black circles. f) Representative dI/dV spectra acquired on O_S of $MoS_{2-x}O_x$ and pristine MoS_2. Set points: 1.1 V, 50 pA.

From our STM images, it shows clearly that the substitutional sites are predominantly on the top S layer of $MoS_{2-x}O_x$. The O-atom density is estimated to be in the range of 10^{13}–10^{14} cm^{-2}. Compared to the pristine MoS_2, the introduction of O_S atoms into it clearly modifies its local electronic structure, evidenced from our STS measurements. Figure 3f shows the dI/dV spectra taken on O_S sites in monolayer $MoS_{2-x}O_x$ together with a control spectrum from pristine MoS_2 (Figure S10, Supporting Information). The measured electronic bandgap of pristine MoS_2 is ≈2.25 eV and the bandgap reduced to ≈1.75 eV of $MoS_{2-x}O_x$ sample ($F_{O2} = 6$ sccm). In general, sulfur vacancies would introduce in-gap states in STS spectra;[33,34] while there are no obvious in-gap states observed in the measured STS spectra, suggesting that oxygen dopants are in a form of substitution chalcogen atoms in our CVD grown monolayer $MoS_{2-x}O_x$ samples and this substitutional doping can effectively modulate their bandgaps. Further, we carried out atomic structure characterizations of as-grown $MoS_{2-x}O_x$ samples with different doping levels as shown in **Figure 4**. Though it is difficult to distinguish the light substitutional atoms of O_S (S—O) and S vacancy (S—)
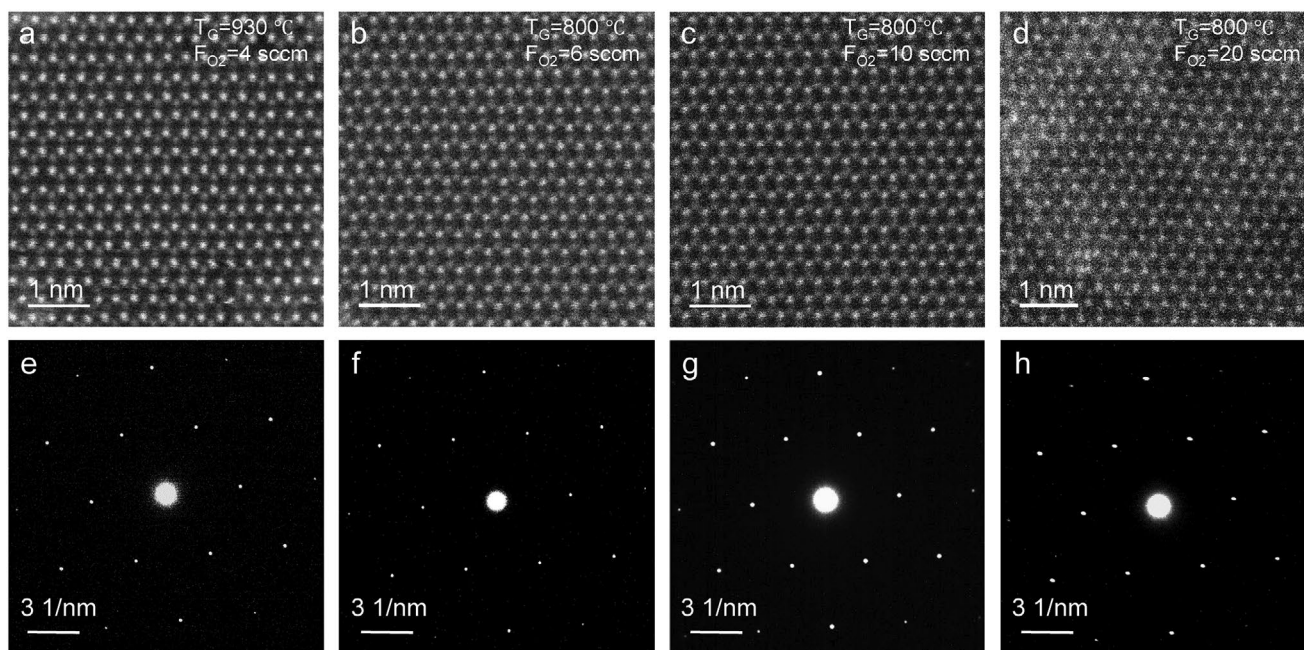
ADVANCED
SCIENCE NEWS
www.advancedsciencenews.com

NANO · MICRO
small
www.small-journal.com

Figure 4. The atomic structural integrity of $MoS_{2-x}O_x$ with increased oxygen doping levels. a–d) As-recorded high resolution ADF-STEM images and e–h) SAED patterns of $MoS_{2-x}O_x$ samples.

due to their relatively weak intensity contrast (Figures S12 and S13, Supporting Information),[35] the overall structural integrity and periodical atomic structure of 2H phase still maintain even at high doping levels as confirmed by high-resolution STEM images (Figure 4a–d; Figure S14, Supporting Information) and selected area electron diffraction (SAED) pattern (Figure 4e–h), which indicate that our doping strategy is non-destructive technique for realizing controllable doping in MoS_2 crystal lattice.

As mentioned above, the oxygen substitutional doping in MoS_2 can significantly affect their electronic properties. We also fabricated FETs based on these $MoS_{2-x}O_x$ monolayers to study their electronic transport properties as shown in **Figure 5**a. Refer to the Experimental Section and Figure S15 (Supporting Information) for details on the device structure and fabrication. Mechanical exfoliated few-layer graphene (FLG) was used as the source/drain and gate electrodes since graphene contact[36,37] has low contact resistance (R_c) of 2.96 kΩ μm as confirmed in Figure S16 of the Supporting Information. Thin hBN flakes with atomically smooth surfaces and free of dangling bonds were used as the dielectric layers to effectively avoid impurity scatterings and trapped charges.[38] Figure 5b,c shows output ($I_{ds}–V_{ds}$) and transfer ($I_{ds}–V_g$) curves, respectively, of a typical $MoS_{2-x}O_x$ device (F_{O2} = 6 sccm). The on-current density (I_{ds}/W) is as high as ≈90 μA μm^{-1}. The linear $I_{ds}–V_{ds}$ characteristics at small biases suggest an excellent contact between $MoS_{2-x}O_x$ and FLG. The saturation characteristics of $I_{ds}–V_{ds}$ at large biases and wide range tunable threshold voltages are important features when interconnecting them for integrated circuits. High on/off ratio of ≈4.5 × 10^9, low off-current ≈100 fA, and ideal subthreshold swing (SS) of 80 mV dec^{-1} can also be achieved in these devices, indicating outstanding device performances. Figure 5d shows

the transfer curves of several $MoS_{2-x}O_x$ FETs with F_{O2} = 4, 6, 10, and 20 sccm. An obvious shift of subthreshold voltages (V_{th}) by doping (n-type) levels can be clearly seen. We also calculated the field effect mobility (μ_{FE}) of these $MoS_{2-x}O_x$ FETs at different doping levels (Figure 5e). Surprisingly, μ_{FE} can be significantly improved by moderate doping, e.g., from 30 cm^2 V^{-1} s^{-1} at F_{O2} = 4 sccm (which is close to an intrinsic case), to 70 cm^2 V^{-1} s^{-1} at F_{O2} = 6 sccm, and a maximum value of 105 cm^2 V^{-1} s^{-1} can be achieved at F_{O2} = 10 sccm (Figures S17–S21, Supporting Information, for detailed electrical analysis). As the highly conductive phase of $MoS_{2-x}O_x$ from O_S substitutional doping could be formed into MoS_2 lattice,[9,14] the electronic behavior of doped MoS_2 films could be modulated, and the sheet conductance and associated field effect mobility (μ_{FE}) could be enhanced with appropriate doping levels (F_{O2} ≤ 10 sccm) as shown in Figure 5e and Figure S22 (Supporting Information). At heavy doping levels (F_{O2} ≥ 20 sccm), the defects and visible damages (Figure 1g) prone to form on the $MoS_{2-x}O_x$ basal plane and serve as the main carrier scattering centers, thus degrading its electronic quality. Indeed, an abrupt dropping of μ_{FE} when F_{O2} > 20 sccm was observed. Furthermore, SS of devices also increases gradually due to the enhanced oxygen doping concentration (Figure 5d). As highlighted in Figure 5f, these moderate doped $MoS_{2-x}O_x$ monolayers show much higher mobilities and on/off ratios than the intrinsic monolayer or few layer MoS_2.[3,39–42]

Based on these high-quality $MoS_{2-x}O_x$ monolayers, we also fabricated complexed logic gates. **Figure 6**a–d shows as-fabricated inverters, NAND, NOR, and AND gates by integrating 2, 3, 3, and 5 FETs, respectively. The output voltage of an inverter has a sharp switching characteristic when sweeping the input voltage (Figure 6e). The voltage gain is 90 at V_{dd} = 5 V, which is superior to pristine MoS_2.[43] Logic functions of NAND, NOR,
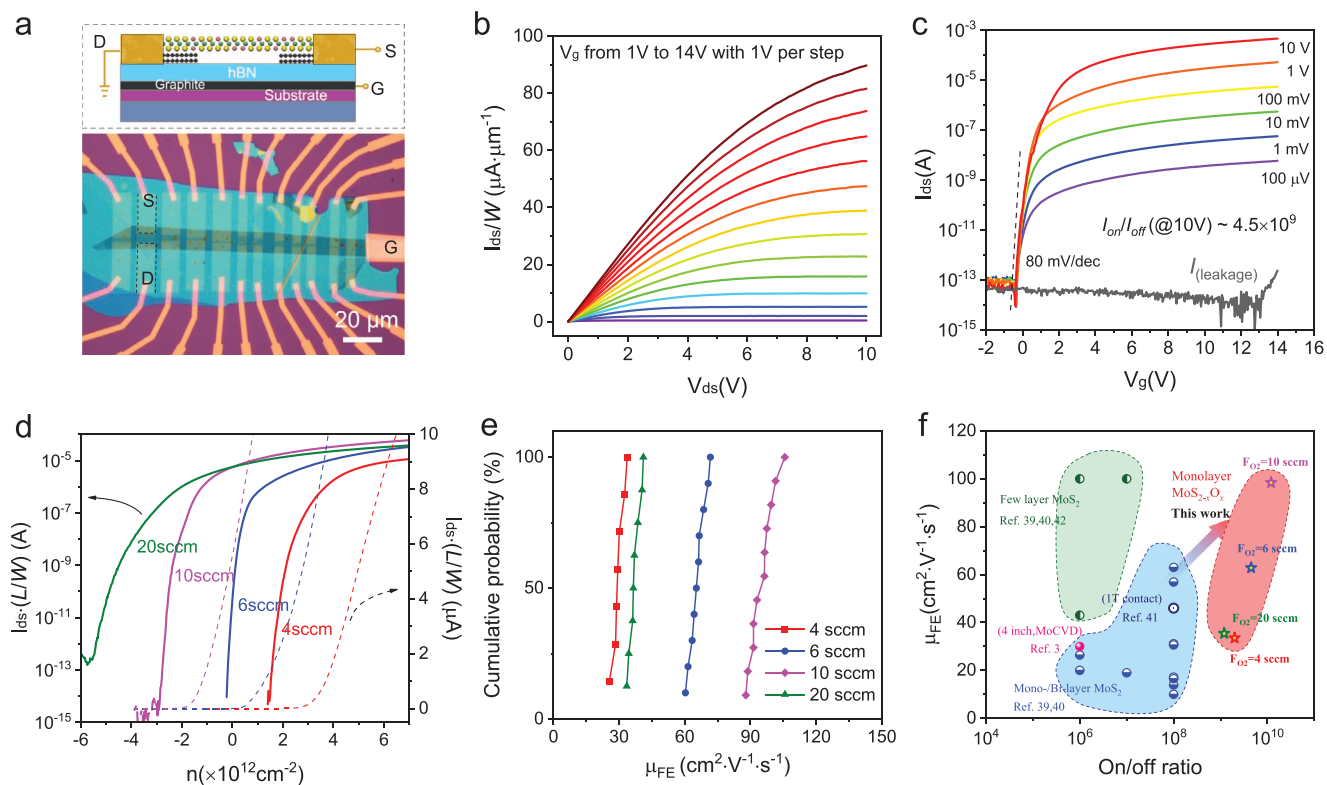
Figure 5. Electrical performances of MoS$_{2-x}$O$_x$ FETs. a) Cross-section schematic illustration and optical image of MoS$_{2-x}$O$_x$ FETs with few-layer graphene (FLG) contact. b,c) Output and transfer curves of a MoS$_{2-x}$O$_x$ device with F$_{O2}$ = 6 sccm. Channel length/width (L/W) is 5/5 μm and hBN thickness (t) is 31 nm. d) Normalized transfer curves with 1 V bias as a function of carrier density (n = C$_i$ V$_g$) of MoS$_{2-x}$O$_x$ FETs with different oxygen doping levels. Solid/dashed lines correspond to left/right panels in logarithm/linear scales. e) Device mobility (μ$_{FE}$) of MoS$_{2-x}$O$_x$ FETs at different oxygen doping levels. f) Comparisons of μ$_{FE}$ and on/off ratio with literature values.

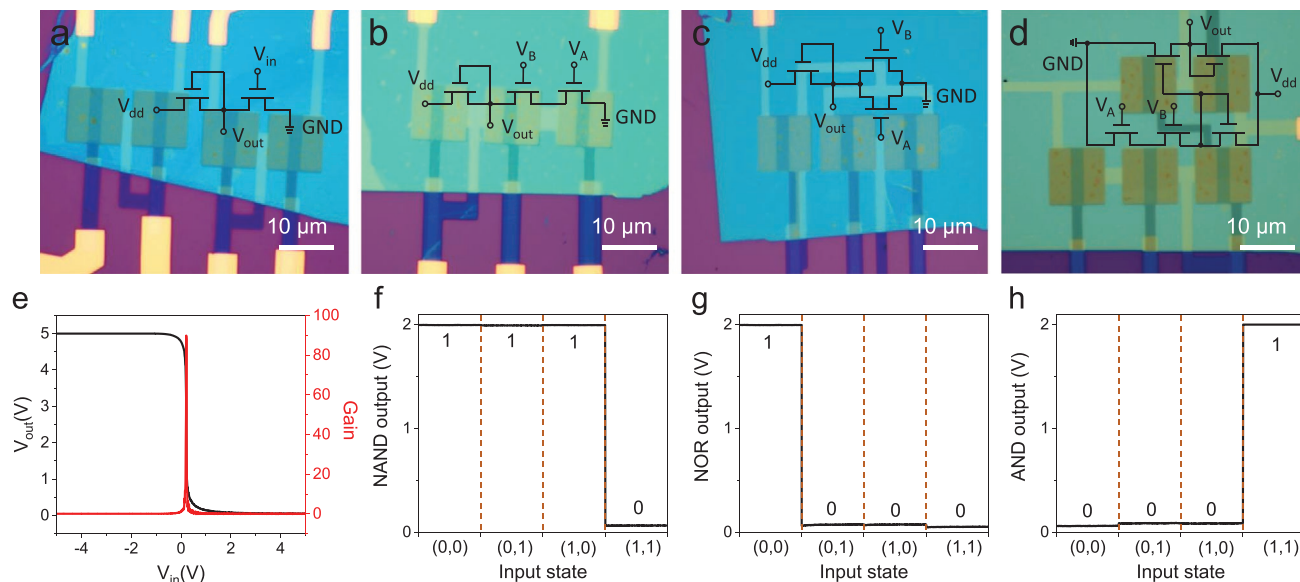**Figure 6.** Demonstration of MoS$_{2-x}$O$_x$ logic gates devices. a–d) Optical images of (a) inverter, (b) NAND, (c) NOR, (d) AND gates with MoS$_{2-x}$O$_x$ (F$_{O2}$ = 6 sccm) as channel materials. Insets are corresponding schematics of logic gates. e) Output voltage V$_{out}$ (left axis) and voltage gain (right axis) as a function of input voltages V$_{in}$ with V$_{dd}$ = 5 V. f–h) Output voltages of the logic NAND (f), NOR (g), and AND (h) gates at four typical input states with V$_{dd}$ = 2 V. "0" and "1" labels represent the low and high binary output states, individually.

and AND could be reliably realized at four typical input states (V_A = 0 (0 V) or 1 (2 V), V_B = 0 or 1) as shown in Figure 6f–h. These results suggest that these $MoS_{2-x}O_x$ monolayers with tunable electronic properties could serve as promising 2D building blocks for novel electronics with better performances than that of the intrinsic MoS_2 monolayers.

3. Conclusion

In summary, we developed an effective CVD technique for in situ oxygen doping of monolayer MoS_2 in a controlled manner and oxygen dopants mainly adopt a form of substitution chalcogen atoms in monolayer $MoS_{2-x}O_x$ samples. We found that the oxygen doping leads to a significant modulation on their optical and electronic properties. Greatly improved carrier mobilities and controllable n-type electronic doping effects resulted from optimized oxygen doping levels of $MoS_{2-x}O_x$ were revealed. The $MoS_{2-x}O_x$-based devices behave excellent electronic performances comparing with intrinsic MoS_2 monolayers, suggesting that such high-quality monolayer films could be better alternatives for future electronic applications.

4. Experimental Section

Growth of $MoS_{2-x}O_x$: The growth of monolayer $MoS_{2-x}O_x$ was carried out in a three-temperature zone CVD system (Figure 1a). S powder (Alfa, 99.5%, 8 g) and MoO_3 powder (Alfa, 99.9995%, 30 mg) were loaded in two inner quartz tube before growth and placed at zone I and zone II, and c-plane polished sapphire (or newly exfoliated graphite) was placed at zone III as substrate. Note that sapphire substrates were preannealed in O_2 atmosphere at 1000 °C for 4 h to form atomic flat surfaces. The carrier gas of Ar (40 sccm) and Ar/O_2 (240/0–25 sccm) was fluxed for S power and MoO_3 sources individually. The pressure in the chamber was kept at ≈1 Torr. Temperatures at zone I, zone II, and zone III were 130, 530, and 800–930 °C and maintained for 30–50 min during the growth.

Sample Characterizations and Measurements: Raman and PL spectra were carried out by a micro-Raman spectrometer (Horiba LabRAM HR Evolution) in a confocal backscattering configuration with an excitation laser wavelength of 532 nm, a laser power of 1 mW and spot size of 1 μm^2. The PL mapping was obtained with WiTec (Alpha 300R) Raman microscope with a laser power of 1 mW and step size of 300 nm. The XPS was acquired from Kratos Analytical Axis Ultra system. STM experiments were performed in a homebuilt low temperature-STM system (4.5 K, 10^{-10} Torr) with chemical etched W tip. STM data were processed by using the free WSxM software.[44] The STS spectra were taken by using a lock-in amplifier with a modulation voltage of 20 mV and at a frequency of 677 Hz. STEM characterizations were acquired by an aberration-corrected Nion U-HERMES200 system operated at 60 kV and STEM simulation was carried out by COMPUTEM software. AFM measurements were performed by Asylum Research Cypher S instrument using RTESP-300 tips. All the electrical measurements were carried out in a Janus probe station (base pressure ≈10^{-6} Torr) with Agilent semiconductor parameter analyzer (4156C and B1500, high resolution modules) at room temperature.

DFT Calculations: First-principles calculations were performed for top and bottom O_S atoms in the MoS_2-basal plane by using the Quantum-ESPRESSO software package,[45,46] which is based on the DFT. The ultrasoft pseudopotential[47] and exchange-correlation functional within a generalized gradient approximation of Perdew–Burke–Ernzerh formula have been used.[48] The sampling of Brillouin zone with a 16 × 16 × 1 k-point mesh was used for a 5 × 5 supercell with a vacuum layer of ≈15 Å for simulations.

Supporting Information

Supporting Information is available from the Wiley Online Library or from the author.

Conflict of Interest

The authors declare no conflict of interest.

[1] G. Fiori, F. Bonaccorso, G. Iannaccone, T. Palacios, D. Neumaier, A. Seabaugh, S. K. Banerjee, L. Colombo, *Nat. Nanotechnol.* **2014**, *9*, 768.

[2] Q. H. Wang, K. Kalantar-Zadeh, A. Kis, J. N. Coleman, M. S. Strano, *Nat. Nanotechnol.* **2012**, *7*, 699.

[3] K. Kang, S. Xie, L. Huang, Y. Han, P. Y. Huang, K. F. Mak, C. J. Kim, D. Muller, J. Park, *Nature* **2015**, *520*, 656.

[4] Z. Lin, Y. Liu, U. Halim, M. Ding, Y. Liu, Y. Wang, C. Jia, P. Chen, X. Duan, C. Wang, F. Song, M. Li, C. Wan, Y. Huang, X. Duan, *Nature* **2018**, *562*, 254.

[5] D. Rhodes, S. H. Chae, R. Ribeiro-Palau, J. Hone, *Nat. Mater.* **2019**, *18*, 541.

[6] Y. Gong, H. Yuan, C. L. Wu, P. Tang, S. Z. Yang, A. Yang, G. Li, B. Liu, J. van de Groep, M. L. Brongersma, M. F. Chisholm, S. C. Zhang, W. Zhou, Y. Cui, *Nat. Nanotechnol.* **2018**, *13*, 294.

[7] S. Z. Yang, Y. Gong, P. Manchanda, Y. Y. Zhang, G. Ye, S. Chen, L. Song, S. T. Pantelides, P. M. Ajayan, M. F. Chisholm, W. Zhou, *Adv. Mater.* **2018**, *30*, 1803477.

[8] H. Li, X. Duan, X. Wu, X. Zhuang, H. Zhou, Q. Zhang, X. Zhu, W. Hu, P. Ren, P. Guo, L. Ma, X. Fan, X. Wang, J. Xu, A. Pan, X. Duan, *J. Am. Chem. Soc.* **2014**, *136*, 3756.

ADVANCED
SCIENCE NEWS

www.advancedsciencenews.com

NANO · MICRO

small

www.small-journal.com

[9] J. Jadwiszczak, C. O'Callaghan, Y. Zhou, D. S. Fox, E. Weitz, D. Keane, C. P. Cullen, I. O'Reilly, C. Downing, A. Shmeliov, P. Maguire, J. J. Gough, C. McGuinness, M. S. Ferreira, A. L. Bradley, J. J. Boland, G. S. Duesberg, V. Nicolosi, H. Zhang, *Sci. Adv.* **2018**, *4*, 5031.

[10] F. Zhang, Y. Lu, D. S. Schulman, T. Zhang, K. Fujisawa, Z. Lin, Y. Lei, A. L. Elias, S. Das, S. B. Sinnott, M. Terrones, *Sci. Adv.* **2019**, *5*, 5003.

[11] D. Kiriya, M. Tosun, P. Zhao, J. S. Kang, A. Javey, *J. Am. Chem. Soc.* **2014**, *136*, 7853.

[12] L. Gao, Q. Liao, X. Zhang, X. Liu, L. Gu, B. Liu, J. Du, Y. Ou, J. Xiao, Z. Kang, Z. Zhang, Y. Zhang, *Adv. Mater.* **2020**, *32*, 1906646.

[13] P. D. Fleischauer, J. R. Lince, *Tribol. Int.* **1999**, *32*, 627.

[14] H. Gao, J. Suh, M. C. Cao, A. Y. Joe, F. Mujid, K. H. Lee, S. Xie, P. Poddar, J. U. Lee, K. Kang, P. Kim, D. A. Muller, J. Park, *Nano Lett.* **2020**, *20*, 4095.

[15] S. Barja, S. Refaely-Abramson, B. Schuler, D. Y. Qiu, A. Pulkin, S. Wickenburg, H. Ryu, M. M. Ugeda, C. Kastl, C. Chen, C. Hwang, A. Schwartzberg, S. Aloni, S.-K. Mo, D. Frank Ogletree, M. F. Crommie, O. V. Yazyev, S. G. Louie, J. B. Neaton, A. Weber-Bargioni, *Nat. Commun.* **2019**, *10*, 3382.

[16] B. Schuler, J. H. Lee, C. Kastl, K. A. Cochrane, C. T. Chen, S. Refaely-Abramson, S. Yuan, E. van Veen, R. Roldan, N. J. Borys, R. J. Koch, S. Aloni, A. M. Schwartzberg, D. F. Ogletree, J. B. Neaton, A. Weber-Bargioni, *ACS Nano* **2019**, *13*, 10520.

[17] A. W. Robertson, Y. C. Lin, S. Wang, H. Sawada, C. S. Allen, Q. Chen, S. Lee, G. D. Lee, J. Lee, S. Han, E. Yoon, A. I. Kirkland, H. Kim, K. Suenaga, J. H. Warner, *ACS Nano* **2016**, *10*, 10227.

[18] J. Peto, T. Ollar, P. Vancso, Z. I. Popov, G. Z. Magda, G. Dobrik, C. Hwang, P. B. Sorokin, L. Tapaszto, *Nat. Chem.* **2018**, *10*, 1246.

[19] S. Susarla, A. Kutana, J. A. Hachtel, V. Kochat, A. Apte, R. Vajtai, J. C. Idrobo, B. I. Yakobson, C. S. Tiwary, P. M. Ajayan, *Adv. Mater.* **2017**, *29*, 1702457.

[20] Y. Gong, Z. Liu, A. R. Lupini, G. Shi, J. Lin, S. Najmaei, Z. Lin, A. L. Elías, A. Berkdemir, G. You, H. Terrones, M. Terrones, R. Vajtai, S. T. Pantelides, S. J. Pennycook, J. Lou, W. Zhou, P. M. Ajayan, *Nano Lett.* **2014**, *14*, 442.

[21] J. Zhou, J. Lin, X. Huang, Y. Zhou, Y. Chen, J. Xia, H. Wang, Y. Xie, H. Yu, J. Lei, D. Wu, F. Liu, Q. Fu, Q. Zeng, C. H. Hsu, C. Yang, L. Lu, T. Yu, Z. Shen, H. Lin, B. I. Yakobson, Q. Liu, K. Suenaga, G. Liu, Z. Liu, *Nature* **2018**, *556*, 355.

[22] N. Kang, H. P. Paudel, M. N. Leuenberger, L. Tetard, S. I. Khondaker, *J. Phys. Chem. C* **2014**, *118*, 21258.

[23] S. I. Khondaker, M. R. Islam, *J. Phys. Chem. C* **2016**, *120*, 13801.

[24] J. Xie, J. Zhang, S. Li, F. Grote, X. Zhang, H. Zhang, R. Wang, Y. Lei, B. Pan, Y. Xie, *J. Am. Chem. Soc.* **2013**, *135*, 17881.

[25] Q. Ji, Y. Zhang, Y. Zhang, Z. Liu, *Chem. Soc. Rev.* **2015**, *44*, 2587.

[26] W. Chen, J. Zhao, J. Zhang, L. Gu, Z. Yang, X. Li, H. Yu, X. Zhu, R. Yang, D. Shi, X. Lin, J. Guo, X. Bai, G. Zhang, *J. Am. Chem. Soc.* **2015**, *137*, 15632.

[27] H. Yu, M. Liao, W. Zhao, G. Liu, X. J. Zhou, Z. Wei, X. Xu, K. Liu, Z. Hu, K. Deng, S. Zhou, J. A. Shi, L. Gu, C. Shen, T. Zhang, L. Du, L. Xie, J. Zhu, W. Chen, R. Yang, D. Shi, G. Zhang, *ACS Nano* **2017**, *11*, 12001.

[28] K. Liu, W. Zhang, Y. Lee, Y. Lin, M. Chang, C. Su, C. Chang, H. Li, Y. Shi, H. Zhang, C. Lai, L. Li, *Nano Lett.* **2012**, *12*, 1538.

[29] T. Y. Ko, A. Jeong, W. Kim, J. Lee, Y. Kim, J. E. Lee, G. H. Ryu, K. Park, D. Kim, Z. Lee, M. H. Lee, C. Lee, S. Ryu, *2D Mater.* **2017**, *4*, 014003.

[30] M. A. Baker, R. Gilmore, C. Lenardi, W. Gissler, *Appl. Surf. Sci.* **1999**, *150*, 255.

[31] L. Seguin, M. Figlarz, R. Cavagnat, J.-C. Lassegues, *Spectrochim. Acta* **1995**, *51*, 1323.

[32] F. D. Hardcastle, I. E. Wachs, *J. Raman. Spectrosc.* **1990**, *21*, 683.

[33] B. Schuler, D. Y. Qiu, S. Refaely-Abramson, C. Kastl, C. T. Chen, S. Barja, R. J. Koch, D. F. Ogletree, S. Aloni, A. M. Schwartzberg, J. B. Neaton, S. G. Louie, A. Weber-Bargioni, *Phys. Rev. Lett.* **2019**, *123*, 076801.

[34] P. Vancso, G. Z. Magda, J. Peto, J. Y. Noh, Y. S. Kim, C. Hwang, L. P. Biro, L. Tapaszto, *Sci. Rep.* **2016**, *6*, 29726.

[35] O. L. Krivanek, M. F. Chisholm, V. Nicolosi, T. J. Pennycook, G. J. Corbin, N. Dellby, M. F. Murfitt, C. S. Own, Z. S. Szilagyi, M. P. Oxley, S. T. Pantelides, S. J. Pennycook, *Nature* **2010**, *464*, 571.

[36] L. Xie, M. Liao, S. Wang, H. Yu, L. Du, J. Tang, J. Zhao, J. Zhang, P. Chen, X. Lu, G. Wang, G. Xie, R. Yang, D. Shi, G. Zhang, *Adv. Mater.* **2017**, *29*, 1702522.

[37] X. Cui, G. H. Lee, Y. D. Kim, G. Arefe, P. Y. Huang, C. H. Lee, D. A. Chenet, X. Zhang, L. Wang, F. Ye, F. Pizzocchero, B. S. Jessen, K. Watanabe, T. Taniguchi, D. A. Muller, T. Low, P. Kim, J. Hone, *Nat. Nanotechnol.* **2015**, *10*, 534.

[38] C. R. Dean, A. F. Young, I. Meric, C. Lee, L. Wang, S. Sorgenfrei, K. Watanabe, T. Taniguchi, P. Kim, K. L. Shepard, J. Hone, *Nat. Nanotechnol.* **2010**, *5*, 722.

[39] B. Radisavljevic, A. Kis, *Nat. Mater.* **2013**, *12*, 815.

[40] S. L. Li, K. Wakabayashi, Y. Xu, S. Nakaharai, K. Komatsu, W. W. Li, Y. F. Lin, A. Aparecido-Ferreira, K. Tsukagoshi, *Nano Lett.* **2013**, *13*, 3546.

[41] R. Kappera, D. Voiry, S. E. Yalcin, B. Branch, G. Gupta, A. D. Mohite, M. Chhowalla, *Nat. Mater.* **2014**, *13*, 1128.

[42] S. Kim, A. Konar, W. S. Hwang, J. H. Lee, J. Lee, J. Yang, C. Jung, H. Kim, J. B. Yoo, J. Y. Choi, Y. W. Jin, S. Y. Lee, D. Jena, W. Choi, K. Kim, *Nat. Commun.* **2012**, *3*, 1011.

[43] H. Wang, L. Yu, Y. H. Lee, W. Fang, A. Hsu, P. Herring, M. Chin, M. Dubey, L. J. Li, J. Kong, T. Palacios, *Int. Electron Devices Meeting, 2012 (IEDM 2012), San Francisco, CA, USA*, IEEE, CA **2012**, p. 4.6.1.

[44] I. Horcas, R. Fernandez, J. M. Gomez-Rodriguez, J. Colchero, J. Gomez-Herrero, A. M. Baro, *Rev. Sci. Instrum.* **2007**, *78*, 013705.

[45] P. Giannozzi, S. Baroni, Bonini, N. M. Calandra, R. Car, C. Cavazzoni, D. Ceresoli, G. L. Chiarotti, M. Cococcioni, I. Dabo, A. Dal Corso, S. de Gironcoli, S. Fabris, G. Fratesi, R. Gebauer, U. Gerstmann, C. Gougoussis, A. Kokalj, M. Lazzeri, L. Martin-Samos, N. Marzari, F. Mauri, R. Mazzarello, S. Paolini, A. Pasquarello, L. Paulatto, C. Sbraccia, S. Scandolo, G. Sclauzero, A. P. Seitsonen, A. Smogunov, P. Umari, R. M. Wentzcovitch, *J. Phys.: Condens. Matter* **2009**, *21*, 395502.

[46] P. Giannozzi, O. Andreussi, T. Brumme, O. Bunau, M. B. Nardelli, M. Calandra, R. Car, C. Cavazzoni, D. Ceresoli, M. Cococcioni, N. Colonna, I. Carnimeo, A. Dal Corso, S. de Gironcoli, P. Delugas, R. A. DiStasio, A. Ferretti, A. Floris, G. Fratesi, G. Fugallo, R. Gebauer, U. Gerstmann, F. Giustino, T. Gorni, J. Jia, M. Kawamura, H. Y. Ko, A. Kokalj, E. Kucukbenli, M. Lazzeri, M. Marsili, N. Marzari, F. Mauri, N. L. Nguyen, H. V. Nguyen, A. Otero-de-la-Roza, L. Paulatto, S. Ponce, D. Rocca, R. Sabatini, B. Santra, M. Schlipf, A. P. Seitsonen, A. Smogunov, I. Timrov, T. Thonhauser, P. Umari, N. Vast, X. Wu, S. Baroni, *J. Phys.: Condens. Matter* **2017**, *29*, 465901.

[47] D. Vanderbilt, *Phys. Rev. B: Condens. Matter Mater. Phys.* **1990**, *41*, 7892.

[48] J. P. Perdew, K. Burke, M. Ernzerhof, *Phys. Rev. Lett.* **1996**, *77*, 3865.

2004276 (8 of 8)